Maria Sklodowska-Curie Actions (MSCA)
Innovative Training Networks (ITN)
H2020-MSCA-ITN-2018
Grant number 813137

Project number 813137

URBASIS-EU
New challenges for Urban Engineering Seismology

DELIVERABLES

Work Package: WP1
Number: D1.1 – Magnitude dependent stress-drop models of European earthquakes

Authors:	**Yen, Ming-Hsuan**	(GFZ)
Co-Authors:	Cotton, Fabrice	(GFZ)
	Bindi, Dino	(GFZ)
Reviewers	Edwards, Benjamin	(UoL)
	Drouet, Stéphane	(FUGRO)

Approval	Management Board
Status	Final Version
Dissemination level	Public
Delivery deadline	31.10.2020
Submission date	15.12.2020
Intranet path	https://urbasis-eu.osug.fr/Scientific-Reports-157

Index

D1.1 – Magnitude dependent stress-drop models (and regional variations) of European earthquakes (focus on the stable continental part of Europe)

Introduction

Stress drop is a fundamental parameter in the description of earthquake source-scaling properties and related ground-motion shaking. It can be defined as two types as "Static stress drop", and "Dynamic stress drop". Static stress drop provides hints on the scaling of the static parameters and static measure describing the average stress released on the fault before and after rupture (Kanamori, 1977; Hanks, 1979; Boore, 1983). Our study will focus on the dynamic stress drop (Brune, 1970, 1971), which accounts for the evolution of stress and is a key parameter in the estimation of strong ground motion, as it controls the level of peak ground acceleration (Hanks and Johnson, 1976). It determines the position of the corner frequency and the height of the high-frequency plateau in the Fourier amplitude spectrum of acceleration.

Seismic stress drop has been identified by the earthquake source spectrum (Aki, 1967; Brune, 1970, 1971). Aki (1967) showed the earthquake source spectrum (the Fourier amplitude spectrum of displacement) has several features (**Figure 1**):

(1) the spectrum amplitude at low frequencies is nearly constant, and its spectral level at zero frequency is proportional to the seismic moment M_0 and to 10^{M_w};

(2) the decay slope is as f^{-2} at high frequencies beyond a corner frequency f_c;

(3) under the assumption of self-similarity (Aki, 1967), the product of the seismic moment and corner frequency cubed is a constant.

Brune (1970, 1971) proposed a model that described the relation between the corner frequency and source radius r. Assuming a circular crack model with uniform stress drop, the source radius is related to the corner frequency through the following equation (Brune 1970; Madariaga, 1976):

$$r = \frac{kV_s}{f_c} \qquad (1)$$

where the constant *k* in equation (1) depends on the assumed rupture model (*k*=0.38 in this study) and V_s is the shear-wave velocity. It has been used in numerous studies to estimate source dimensions from measured corner frequencies, mostly for small to moderate earthquakes. The Brune'smodel leads to a Fourier amplitude spectrum which has an ω^2-shape, and is similar to the Haskell (1964) model. The stress drop $\Delta\sigma$ can be derived from the seismic moment M_o and the source radius using the following equation (Eshelby, 1957; Keilis-Borok, 1959):

$$M_0 = \frac{16}{7}\Delta\sigma r^3 \qquad (2)$$

For the scaling relationship of the stress drop with earthquake size, several assumptions have been applied. Variability in $\Delta\sigma$ is apparent and due to both the different adopted methodologies and the model-dependent assumptions. The scaling of stress drop with the earthquake size is still a controversial issue in seismology and earthquake source mechanics. Some studies advocated that there is no dependence of stress drops on seismic moment (Ide and Beroza, 2001; Ide et al., 2003; Baltay et al., 2010, 2011). Other studies found a systematic increase of these parameters with earthquake size (Izutani and Kanamori, 2001; Mayeda et al., 2005; Harrington and Brodsky, 2009). Denolle and Shearer (2016) showed that observed earthquakes are not self-similar because their source geometry and spectral shapes vary with earthquake size. **Figure 2** shows a recent synthesis of the scaling of stress drop with seismic moment for earthquakes from different tectonic settings (Cocco et al., 2016). According to this synthesis, stress drops increase with the seismic moment within individual sequences. However, the overall pattern is not showing a clear trend. This suggests that homogenous and high-quality stress-drops analysis are still needed.

In this study, we take advantage of the growth of seismological data in Europe to address the following key questions:

(1) Is the stress drop magnitude-dependent in the stable part of Europe?

(2) Is the stress drop depth-dependent in the stable part of Europe?

(3) Do stress drop values show regional variations?

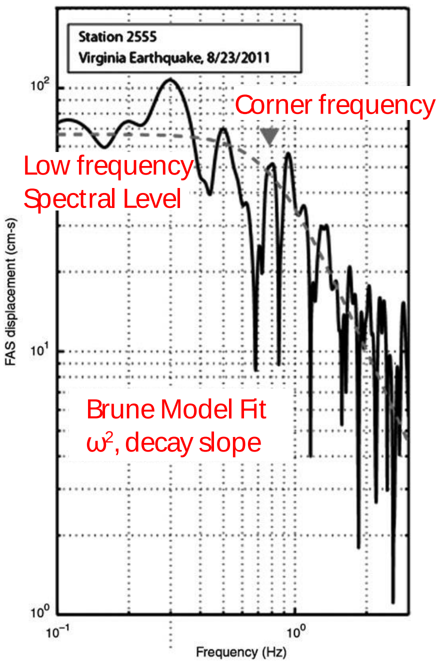

Figure 1. Example of Brune-model fitting the Fourier amplitude spectrum of displacement to determine a corner frequency (red cross) and displacement plateau (Cotton et al., 2013).

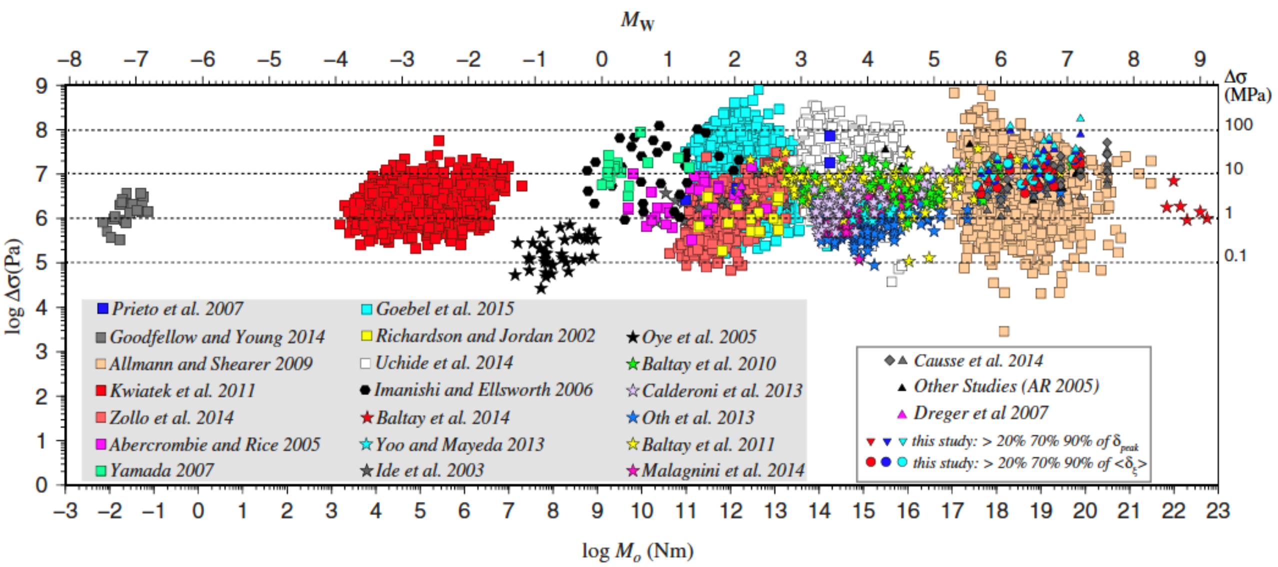

Figure 2. Stress drop scaling with seismic moment for different earthquakes in different tectonic settings (Cocco et al., 2016). Upturned triangles and circles show the average dynamic stress drop estimates performed in Cocco et al. (2016) from stress and slip temporal evolutions. Squares indicate point source estimates of static stress drop obtained by using the Madariaga (1976) relation between corner frequency and source radius; stars identify those computed by using the Brune (1970) law; and hexagons indicate those computed by using the Sato and Hirasawa law. Other estimates from averaged finite source models are indicated with triangles (static stress drop) and diamonds (dynamic stress drop).

Database

In the framework of the activities of ESR1.2, a new database of waveforms relevant to earthquakes occurred in Europe has been created. The data source considered is the EIDA repository, i.e., the European Integrated Data Archive (https://www.orfeus-eu.org/data/eida/), a distributed federation of datacenters established to archive and disseminate seismic waveform and metadata. EIDA is composed by 12 EIDA-nodes (https://www.orfeus-eu.org/data/eida/nodes/) sharing continuous data streams archived in the different centers and accessible using FDSN compliant webservices (http://www.fdsn.org/services). In EIDA, streams from different channel types are stored including, among others, both broad-band data and strong motion data.

To access the data and download the segments of interest, we used the stream2segment tool (https://geofon.gfz-potsdam.de/software/stream2segment/), a suite of python programs facilitating the entire workflow of downloading, inspecting, and processing event-based seismic data by means of a relational database management system as archiving storage. The main steps followed to create the Fourier amplitude spectra for the waveforms stored in the local database is detailed in the following.

Downloading the data

The download process is guided by a seismic event catalog. The event catalog has been created using the event webservice of the International Seismological Center, ISC (http://www.isc.ac.uk/fdsnws/event/1). The largest time span considered is from January 1st, 1990 to May 31st, 2020 and the maximum hypocentral depth was set to 60 km. The download has been split into different chunks covering different geographical areas corresponding to rectangular regions defined by [*longitude min; longitude max; latitude min; latitude max; minimum magnitude*]. In particular, we considered the following regions: [8.05; 19.05;36.5; 45.45; 2.7]; [-12,0; 8.0; 34; 45.45; 2.5]; [-12.0; 26.5; 45.5; 71; 2.0]; [19.0; 46.0; 33.0; 42.5; 2.8]; [19.1; 33.0; 42.6; 45.5; 2.5]. Please note that the magnitude used for the selection is the one provided by the event service and the size of different events is given in terms of different magnitude scales. Moreover, different minimum magnitudes have been set for different regions depending on the level of seismic activity. Starting from the hypocentral locations, stations up to a distance of 5 degrees have been queried for data availability. We download segments 4 minutes long starting 1 minute before the theoretical P-wave arrival time (computed considering the AK135 global velocity model) and selecting the three components of motion from HH, HN, HL, HG, EH channels [following the SEED convention on the channel names, that is, high sampling rate channels from broad band (HH), short period (EH) and strong motion instruments (HN but also HL and HG)]. Counting only segments with data, the data base hosts about 27.9 million segments (over a total of about 52 million) from 178,000 earthquakes recorded by 4,771 stations belonging to 118 either temporary or permanent networks (**Figure 3**).

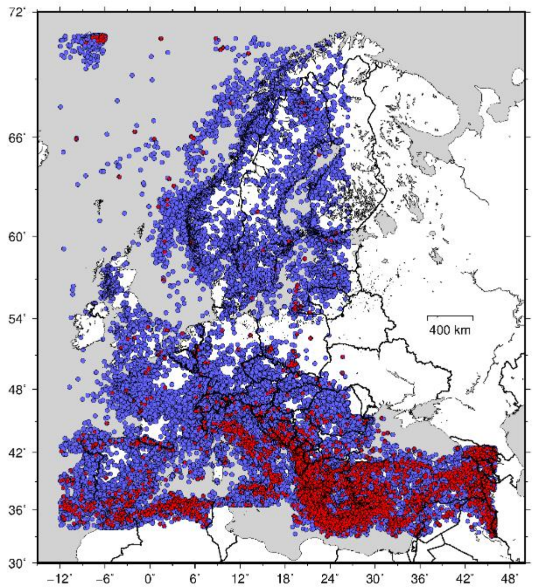

(a)

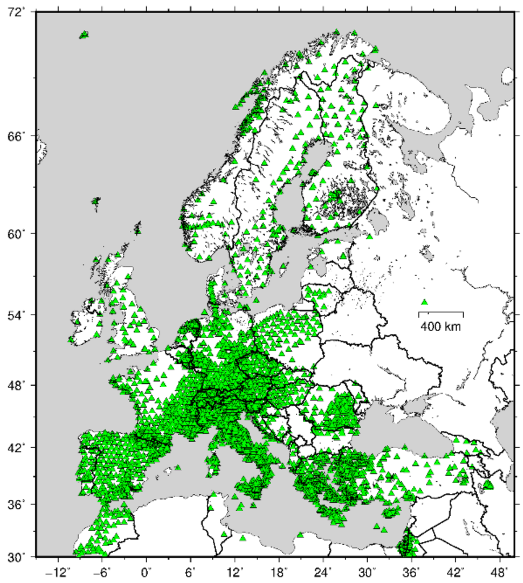

(b)

Figure 3. (a) Locations of earthquakes considered to populate the data base; red symbols indicate events with magnitude larger than 4. (b) Locations of all considered stations.

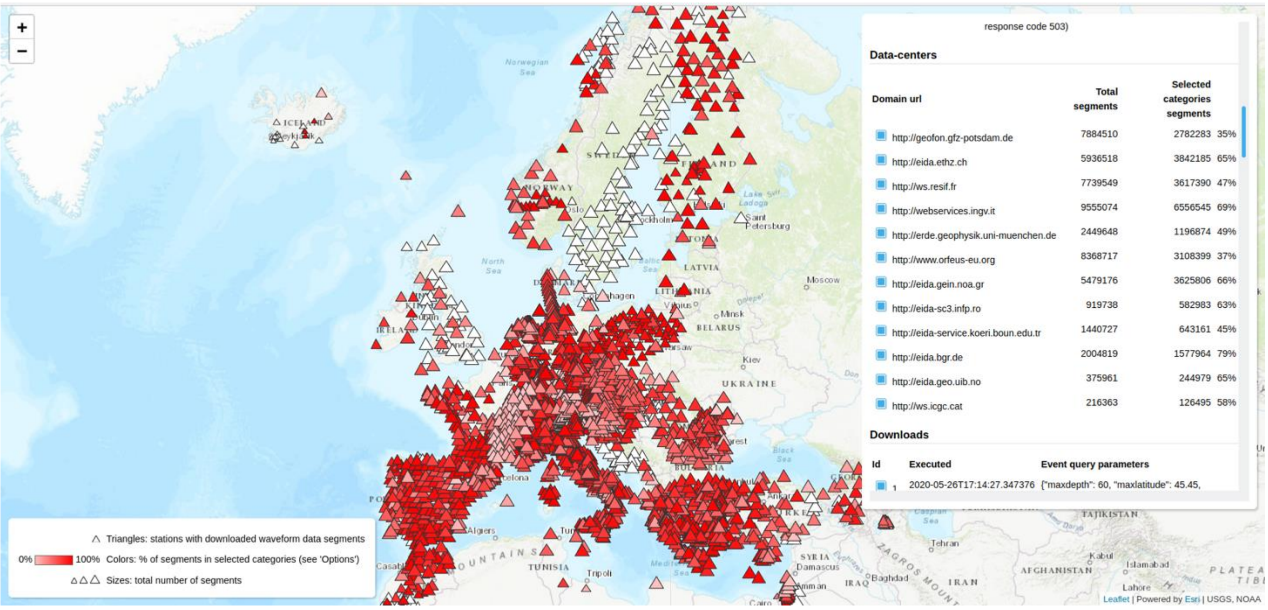

Figure 4. Statistic of the download for the considered stations, where the symbol size is proportional to the total amount of data requested and the intensity of the color is proportional to the fraction of retrieved data over the total amount requested (where white indicates stations for which no segments were provided for example because of restrictions).

Pre-Processing

The segments extracted from the repository are stored in a postgres database, along with metadata information. A customized processing pipeline was applied to each segment using stream2segment. The processing workflow is defined by the following the main steps: 1) check for possible clipped signals by simply comparing the maximum digital count in the trace with the fraction (80%) of the full scale (FS)=($2^{24}-1$) of a 24 bit digitizer; 2) band-pass filter the trace using a zero-phase, 2-poles, Butterworth filter with high pass corner frequency f_H being magnitude dependent and the low pass corner frequency fixed to 90% of the Nyquist. Corner frequency f_H was set to 0.08 Hz for magnitude above 6; to 0.3 for magnitudes between 3 and 6; and to 0.5 Hz for events smaller or equal to 3; 3) the instrumental response is removed in the spectral domain setting the water level regularization to 60, and converted to acceleration; the signal window is defined as the interval between the 2.5% and 97.5% percentile of the cumulative squared acceleration, fixing the minimum duration to 10 s; window with multiple events are discarded based on automatic procedure based on the analysis of the second derivative of the cumulative squared acceleration; signal to noise ratio SNR is computed over different frequency ranges: [fmin,0.15], [0.15,0.25], [0.25,0.4], [0.4,0.65], [0.65,1], [1,1.6], [1.6,2.5], [2.5,3.2], [3.2,4], [4,6.3], [6.3, 10], [10,16], [16,25], [25,fmax], [fmin,fmax] Hz; peak parameters (e.g., peak ground acceleration and velocity; maximum Wood-Anderson amplitude) and Fourier amplitude spectra are evaluated; the output (selected metadata information, SNR values, assessed intensity measures) are written in a tabular file (flat file) or using the Hierarchical Data Format (HDF) (https://support.hdfgroup.org/). Segments with SNR smaller than 2.5 over [fmin,fmax] are no further processed, whereas refinements of the selection criteria by setting different thresholds for different frequency intervals will be application dependent.

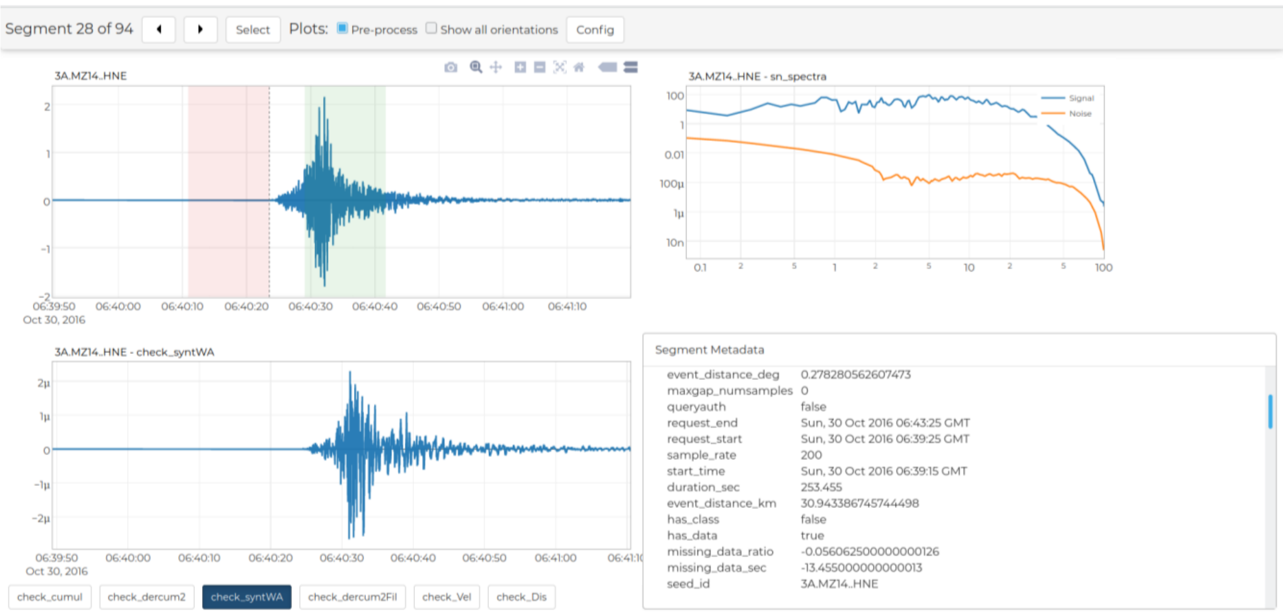

Figure 5. Example of data processing (corrected acceleration time histories; signal and noise spectra; synthetic Wood-Anderson seismogram) for the 2016, Mw 6.5 Norcia earthquake, recorded at station 3A.MZ14.HNE (epicentral distance 31 km).

Data selection and processing

For the test dataset in this deliverable, we extracted a subset of segments to perform preliminary analysis. We considered events that occurred from 1990 to 2016 in central Europe, with magnitude above 3.0, depth shallower than 60 km and selecting recordings from stations located at a maximum hypocentral distance of 2 degrees. The events of a subset are selected in central Europe (5°W, 15°E, 41°N, 57°N). The data set is shown in **Figure 6**, in terms of source-station ray paths. For testing the impact of the regionalization of the spectral decomposition, we split the subset into two, as Case II and Case III: (1) the events mainly located in Italy (latitude less than 46°N), (2) the events mainly located in Germany (latitude greater than 46°N). **Figure 7** shows the hypocentral depth and distance distribution of the overall data set. Please note that this simple regionalization is considered to get first order insights about how regional effects could impact the calibration of seismological models, and to motivate future efforts dealing with more tectonic-based regionalization schemes.

The subset has been assembled with the purpose of developing preliminary analysis over data quality and to set-up the methodologies for the spectral decomposition approach. For the spectral decomposition approach, the Fourier amplitude spectrum (FAS) is the vector sum of two horizontal components, which is independent on the sensor rotation. The geometric mean of the peak ground velocity (PGV) and acceleration (PGA), as generally implemented in ground motion prediction equations, is also computed by selecting segments with minimum SNR over the two horizontal components larger than the applied threshold. For the analysis presented in this report, we consider the frequencies between 0.5 and 20 Hz.

The data selection and processing are applied in two steps. The first step is based on residual analysis with respect to predictions from Ground Motion Prediction Equations (GMPEs) considering the PGV and PGA for Europe and Middle East (Bindi et al., 2014) to detect the presence of outliers, as shown in **Figure 8**. The outlier analysis is using a robust Z-score method applied to the median absolute deviation of residuals. Iglewicz and Hoaglin (1993) suggested that the Z-score for the presence of outliers was greater than 3. According to our data distribution and preliminary testing, the score in this study is set as 100. Ongoing effort is devoted to improve the outlier detection, in particular for segments with smaller than expected amplitudes. An example of the outlier analysis of PGV residual is shown in **Figure 9**. The second step is based on the signal to noise ratio (SNR). We set an additional SNR standard for our selection that the threshold for the frequency band of 0.5-20 Hz is set as 10 (**Figure 10**).

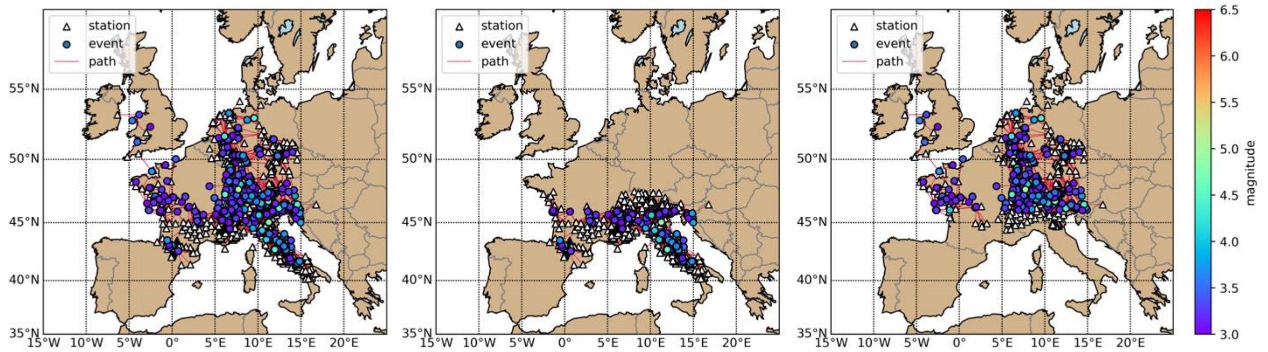

Figure 6. A subset (Case I, II, and III) of segments for preliminary investigations. Events with magnitude above 3 have been selected, and recordings collected from broad band, short period, and strong motion stations.

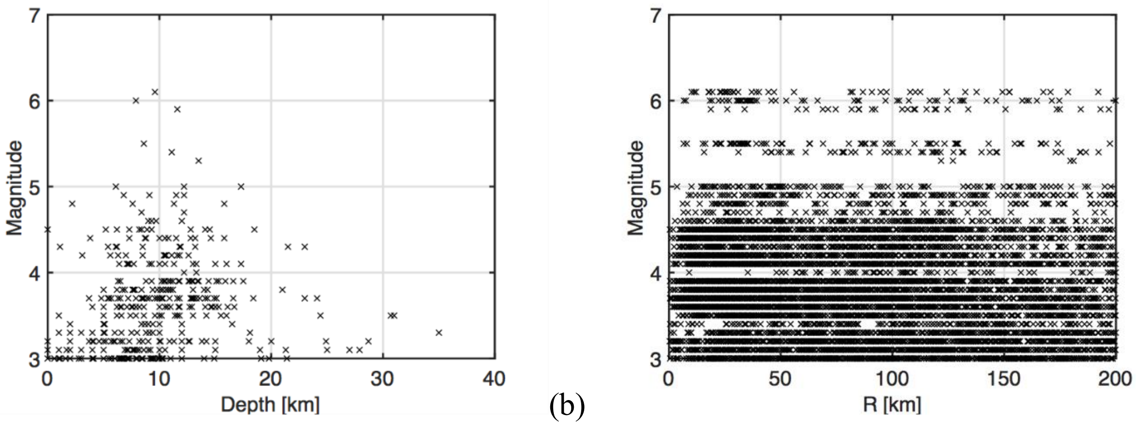

(a) (b)

Figure 7. Earthquakes magnitude as function of (a) depth and (b) hypocentral distance.

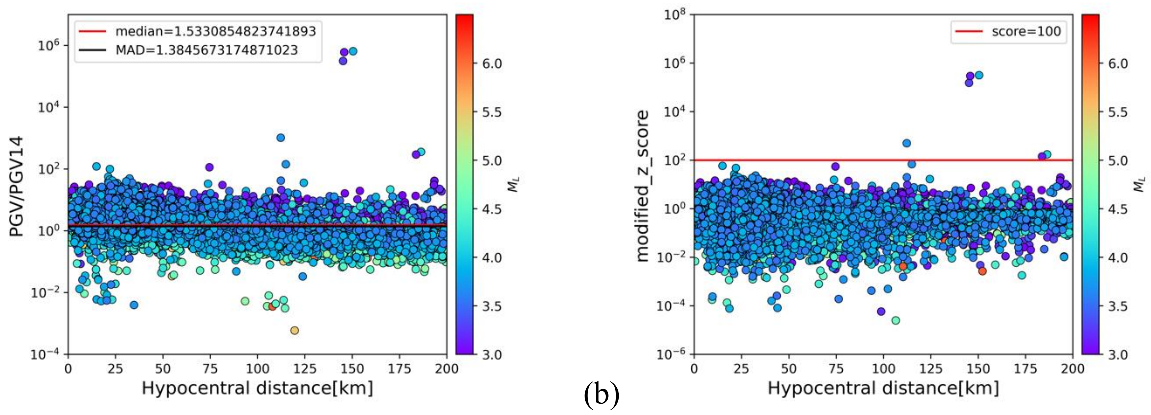

(a) (b)

Figure 8. Analysis for isolating outliers using a robust modified Z-score method applied to the median absolute deviance. (a) Residual of PGV and the respective predictions from Ground Motion Prediction Equations (GMPEs). (b) Z-score of the residual against the hypocentral distance.

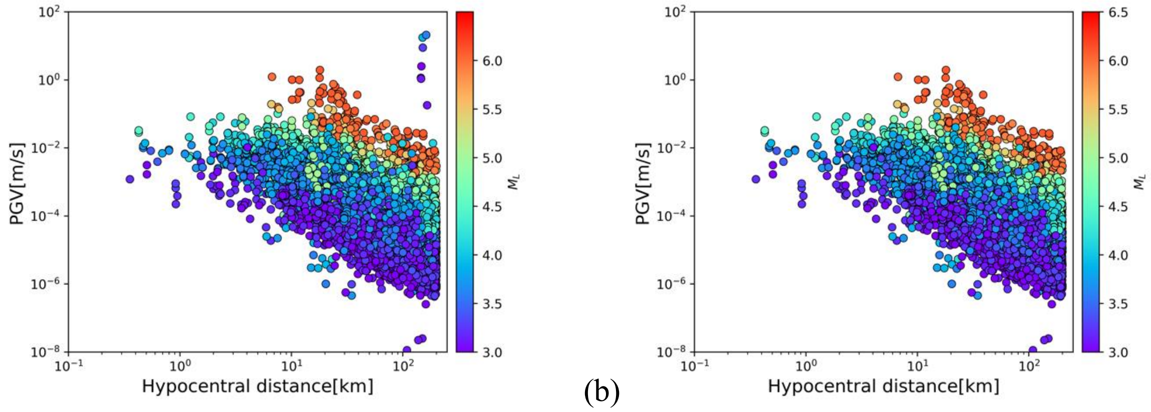

(a) (b)

Figure 9. An example of the outlier analysis of PGV residual. (a) PGV as a function with hypocentral distance before removing the outliers. (b) PGV as a function with hypocentral distance before removing the outliers.

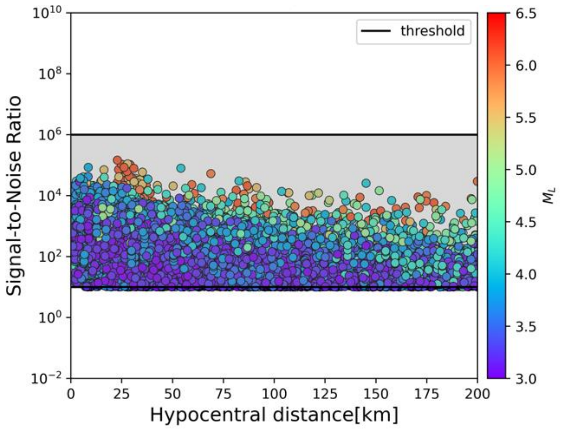

Figure 10. An example of signal-to-noise ratio (SNR) of the subset against hypocentral distance in the frequency range of 0.5-20 Hz. Symbols are color coded with the local magnitude M_L as retrieved from the event catalog.

Methodology

After the correction for the instrumental response considering the full poles and zeros deconvolution and under the hypothesis of linear system, the ground shaking recorded by the seismometer is given by the convolution product of the source, propagation and site amplification factors. Considering the frequency domain and taking the logarithm of each factor, the spectral model can be written as:

$$log_{10}U_{ij}(f,R_{ij}) = log_{10}S_i(f) + log_{10}G(f,R_{ij}) + log_{10}Z_j(f) \quad (3)$$

where U_{ij} is the Fourier spectral amplitude at frequency f of event i recorded at station j, which is located at the hypocentral distance R_{ij}; $S_i(f)$ is the source spectrum of event i; $G(f,R_{ij})$ is the spectral attenuation with distance and Z_j describes the site amplification at station *j*. If the distance range from the minimum to the maximum analyzed hypocentral distances is discretezed into a N_{bin} intervals with nodes at R_n, n=1,…,N_{bin}+1 , then equation (3) can be written as:

$$log_{10}U_{ij}(f,R_{ij}) = \sum_{k=1}^{N_{event}} \delta_{ik}\, log_{10}S_k(f) + a_n log_{10}G_n(f) + a_{n+1} log_{10}G_{n+1}(f) + \sum_{k=1}^{N_{stations}} \delta_{jk}\, log_{10}Z_k(f) \quad (4)$$

Where

$$a_n = (R_{n+1} - R_{ij})/(R_{n+1} - R_n) \\ a_{n+1} = 1 - a_n. \quad (5)$$

are the coefficients for the discretized distances, imposing a liner interpolation between two consecutive nodes, and n is such that $R_n \leqslant R_{ij} < R_{n+1}$. When i and j are iterated over all the values they can assume (i.e., considering all available recordings), equation (4) generates for each frequency a linear system of equations with unknown S_i(f), i=1,…,N_{event}; Z_j(f) with j=1,…,$N_{station}$; G_n(f) with n=1,…,N_{bin}. For each row, the coefficients of the linear system are given by the deltas δ_{ik} and δ_{jk}, assigning value 1 to the columns relevant to event *i* and station *j*, respectively, and 0 to all others; for the distance, the coefficients are a_n, a_{n+1} assigned to the two columns relevant to the discrete distances encompassing R_{ij}. The system has a number of rows (data) equal to the number of records available for frequency *f*, and a number of columns (unknowns) equal to the sum of the number of stations, events, and discrete distances (i.e., N_{event}+$N_{station}$+N_{bin}+1). The over-determined system can be solved in a least-squares sense and the different approaches for finding the solutions are known as generalized inversion technique GIT (e.g., Castro et al., 1990; Oth et al., 2011; Bindi and Kotha, 2020). Since in equation (4) the different unknowns are not described in terms of a-priori functional forms (i.e., seismological models), the approach followed in this study is called non-parametric. Examples of parametric approach to the generalized inversion are given by Edwards et al. (2008), Drouet et al. (2010), Moschetti and Hartzell (2020). Since in the non-parametric approach the spectral shapes of the unknown terms are not shaped, the linear system (4) is solved for each frequency separately.

Despite the fact that the system is over-determined, the linear system generated by equation (4) has two unresolved degrees of freedom linked to trade-offs among the three terms (source, propagation and site). As consequence of the trade-offs, the GIT approach can only provide relative solutions to a priori fixed constraints, implemented as additional rows to the design matrix. Among different possibilities, it is common practice for the non-parametric approach to select a reference distance (generally close to the source region) where the attenuation is set to 1 (i.e., the retrieved source spectra are estimated at the reference distance) and to assume a reference site condition. The reference site condition has an important impact on the interpretation of the results: all the site amplifications are relative to the assumed reference and a site effect common to the sites used as reference set is moved to the sources. A common choice is to select one or more stations which are expect to be exempt from significant local site amplification effects (generally stations installed on rock without significant topographic effects, with relatively flat horizontal to vertical spectral ratios) and constrain the average amplification of the reference stations to an a-priori selected function of frequency. The latter is generally set either to a flat amplification equal to 1 or to the expected effect of the crustal amplification, multiplied by a high-frequency near surface attenuation term (representing the average k_0 for the rock conditions at the reference stations). In this study, we set k_0 to 0.015 s, negleting the contribution of the crustal amplification. It worth noting that by solving equation (4) in one single step (Castro et al., 1990), the spectral attenuation term G(f,R) does not depend on the reference site condition (Oth et al., 2011; Ameri et al., 2020), that is, the selection of the reference site condition plays a fundamental role in resolving the trade-off between source and site terms, when data sets with good level of redundancy are analyzed. Finally, besides the constraints applied to break the trade-offs among the three factors, the requirement that the attenuation with distance solutions are smooth is also added to the design matrix (Castro et al., 1990).

Results

To assess the stability of the inversion results, our test performs 100 bootstrap inversions at each frequency point following the procedure detailed in Parolai et al. (2000, 2004). The GIT inversion we apply is one-step non-parametric approach which isolates the source, site, and path functions directly in one step. We constrain $G(f, R_{ij})$ to a smooth function of distance as well as $G(f, R_0)$=1, with R_0 set equal to 5 km. The constraint of the site response function at each frequency point was set to the average site response computed considering all available stations. The distance range 0-200 km is subdivided into distance bins of 5 km wide to determine the attenuation functions. To obtain site response functions and source spectra relative to the same reference condition, we corrected the ground motion spectra for attenuation by the attenuation curves from the one-step GIT inversion to a reference distance of 5 km and then separate source and site terms.

Attenuation

Figure 11 shows examples of the attenuation functions obtained for six frequencies with the spectral amplitudes corrected for source and site terms as derived from the one-step GIT inversion. The obtained attenuation curves well describe the distance decay of the corrected spectral amplitudes. At given distances (<10km, about 20 km and about 100 km), there are few outliers that will be used in future to refine the outlier detection approach.

Figure 12 shows the attenuation curves by considering 100 bootstrap replications for all 53 frequency points between 0.5 and 20 Hz. In all the cases, the curves generally show a similar decay pattern within the first 5-50 km and start diverging beyond the distance of around 50 km. The attenuation curves for high frequencies decay more rapidly than the ones for low frequencies as expected. The attenuation curves of Case I and II decay faster at distances above 50 km for the high frequency, but those for Case III present a slower decay.

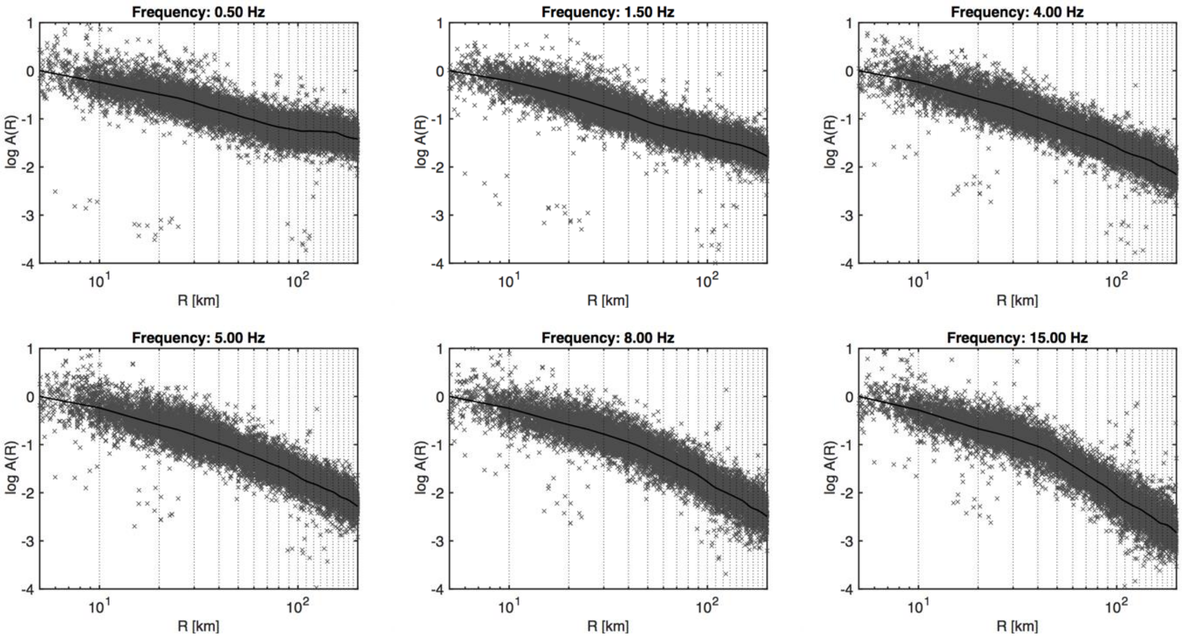

Figure 11. Attenuation function, $\overline{logA(f,R)}$ with R being hypocentral distance, for Case I at six given frequencies. Solid black lines indicate the mean value calculated by bootstrap resampling. The dark gray crosses indicate the recorded spectral amplitudes, corrected for source and site contributions as derived from the GIT inversion.

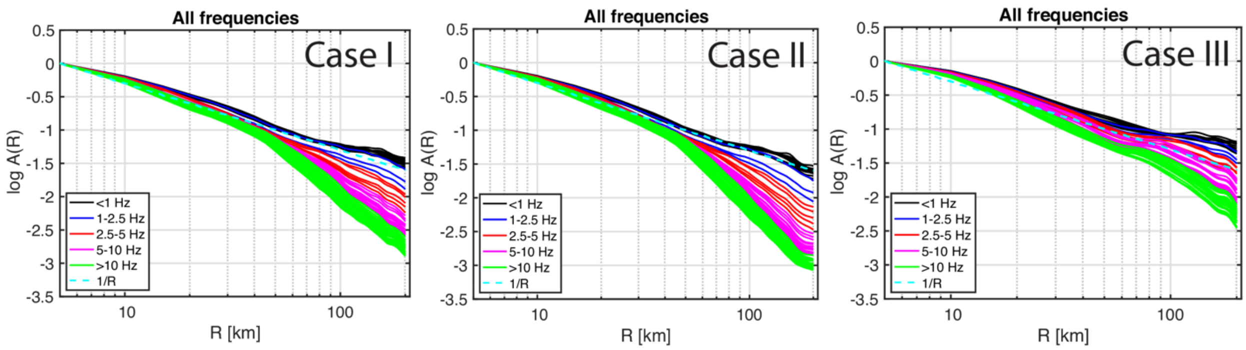

Figure 12. Non-parametric spectral attenuation curves obtained by considering 100 bootstrap replications of the data set. Different colors indicate different frequencies as indicated in the legend.

Source parameters

After determining the attenuation, we corrected the FAS for attenuation and separated them into the source and site response contributions. **Figure 13** shows several examples of source spectra at 5 km reference distance derived from GIT inversion for Case I. The standard deviations for these two examples show that the source spectra estimates are generally stable.

The obtained source spectra are fitted with the ω^2-model (Brune, 1970,1971) are used to determine corner frequency and seismic moment, using nonlinear least squares (Oth et al., 2010):

$$S(f) = (2\pi f)^2 \frac{R^{\theta\phi}F}{4\pi\rho {v_s}^3 R_0} \acute{M}_0 \, with \, \acute{M}_0 = \frac{M_0}{1 + (f/f_C)^2}$$

Where $S(f)$ represents the acceleration source spectrum at the reference distance R_0=5 km. $\dot{M}_0$ denotes the moment-rate spectrum, $R^{\theta\phi}$the average radiation pattern of S-waves set to 0.55 (Boore and Boatwright, 1984), F=2 is the free surface factor, and ρ=2.7 g/cm^3 is the density and v_S=3.3 km/s is the shear-wave velocity near the source.

Stress drop $\Delta\sigma$ was computed following Hanks and Thatcher (1972):

$$\Delta\sigma = 8.5 M_0 \left(\frac{f_C}{V_S}\right)^3$$

Figure 14 shows the corner frequency against the moment magnitude fitting. The relationship expected for a self-similar behavior should show a -1/3 slope and the obtained regression calculated from our data analysis shows a slope which is not far from that theoretical self-similar behavior. The stress drops were computed from the corner frequency, as shown in **Figure 15**. The resulting stress drops are mainly distributed in the range of 1-10 MPa.

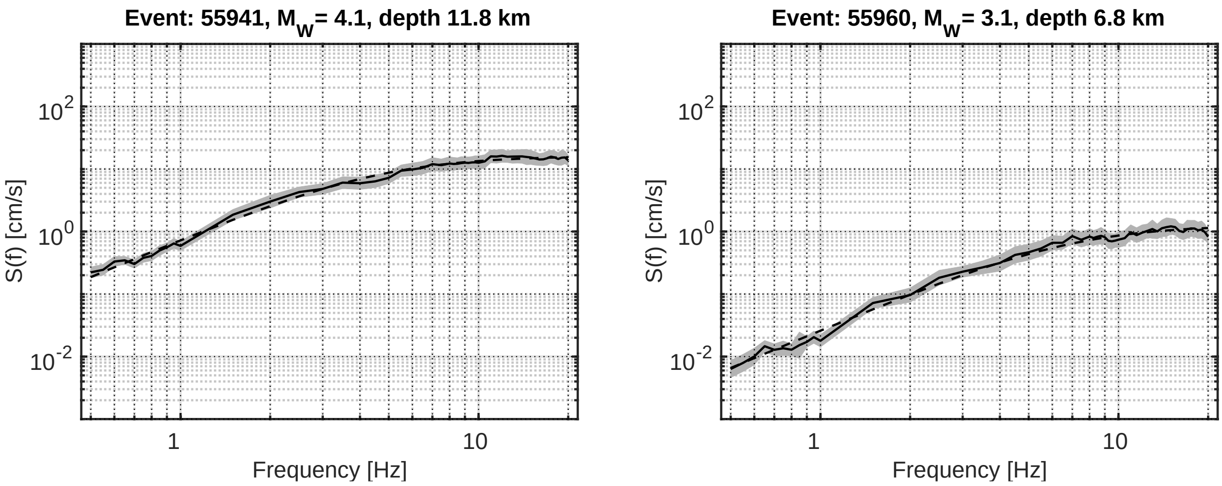

Figure 13. Examples of acceleration source spectra derived from GIT inversion for Case I. Black lines indicate the average value. Gray area indicates the standard deviation of bootstrap samples.

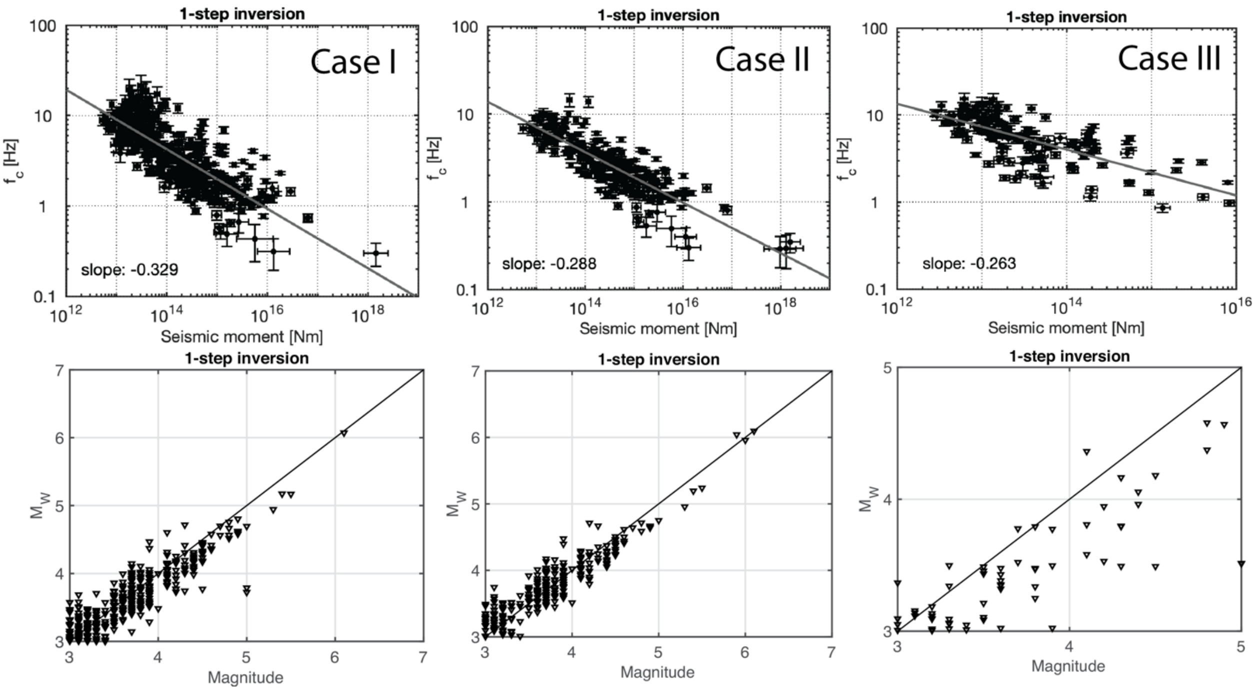

Figure 14. Scaling results of the corner frequency against the seismic moment fitting for three cases. Gray lines indicate the linear regression for all the events.

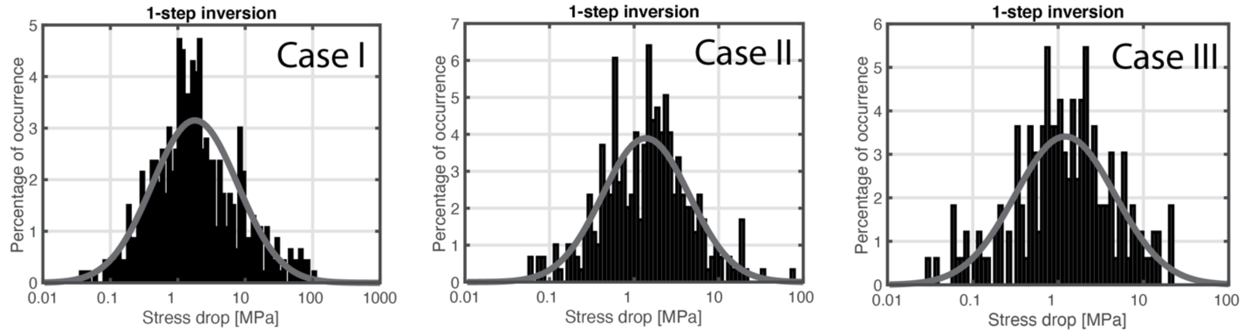

Figure 15. The distribution of the stress drops for three cases.

Discussion

1) Variation with depth

The stress drops obtained in our study show a weak increase with the depth of events (Figure 16) which is consistent with several previous studies (Shearer et al., 2006; Allmann and Shearer, 2007; Drouet et al., 2011; Oth, 2013) as shown on **Figure 17** and **Figure 18**.

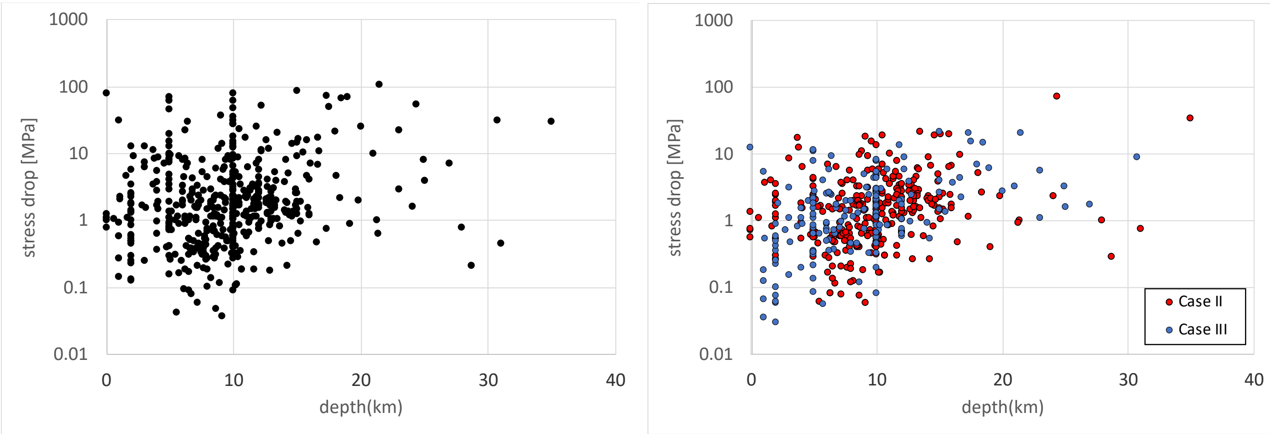

Figure 16. Stress drops obtained in this study and their dependency on depth. Black dots indicate the result of Case I. Red dots indicate the result of Case II. Blue dots indicate the result of Case III.

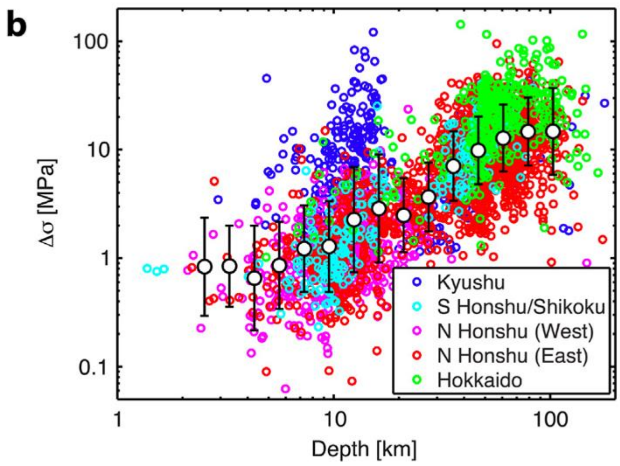

Figure 17. Brune's stress drop scaling with the depths of events in Japan. Color-coded shows the result in different regions (Oth et al., 2013)

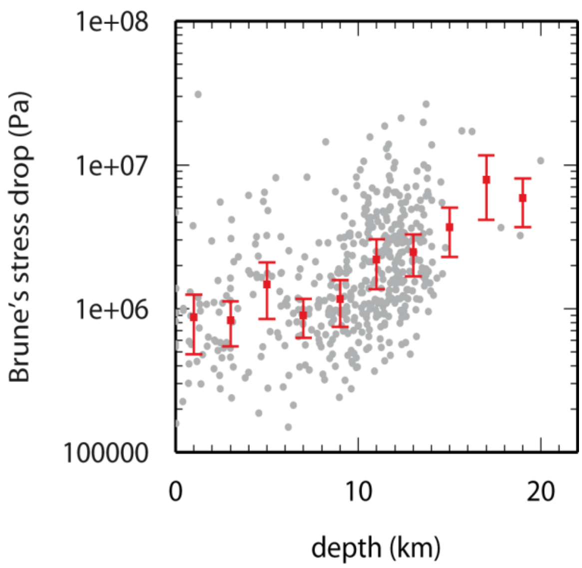

Figure 18. Brune's stress drop scaling with the depths of events in the French West Indies (Drouet et al., 2011).

2) Regionalization

The distribution of the stress drop with the latitude shows that the stress drop is lower in the southern part (Italy) and higher in the northern part (Germany) for the case of the entire region (**Figure 19 and 20**). **Figure 21** shows that the obtained stress drops of Case III show large difference with the one obtained for Case I for the earthquakes located in the stable part of Europe. It may indicate that the attenuation correction of Case I is not suitable for the stable part of Europe which motivate a future regionalization approach to get accurate attenuation functions.

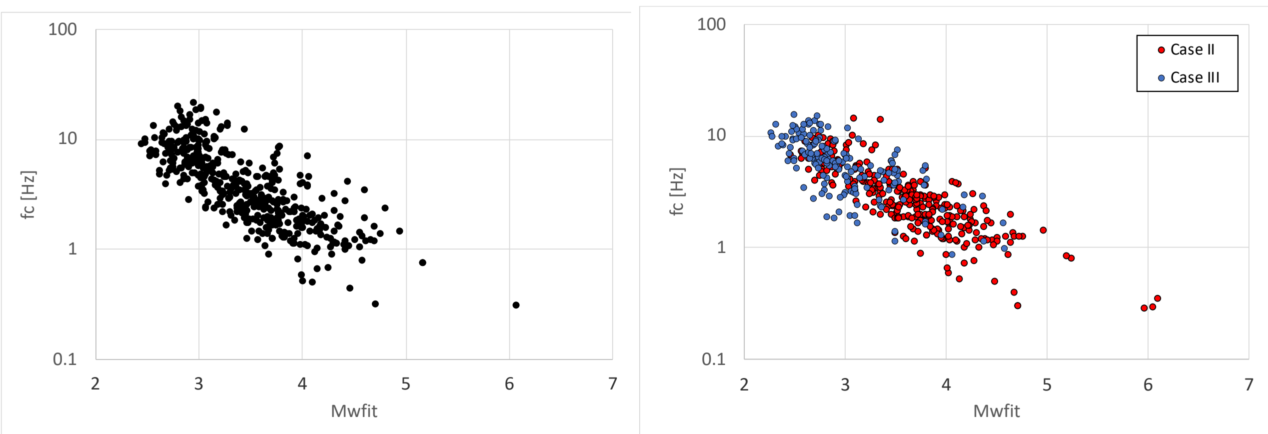

Figure 19. The corner frequency against Mw. Black dots indicate the result of Case I. Red dots indicate the result of Case II. Blue dots indicate the result of Case III.

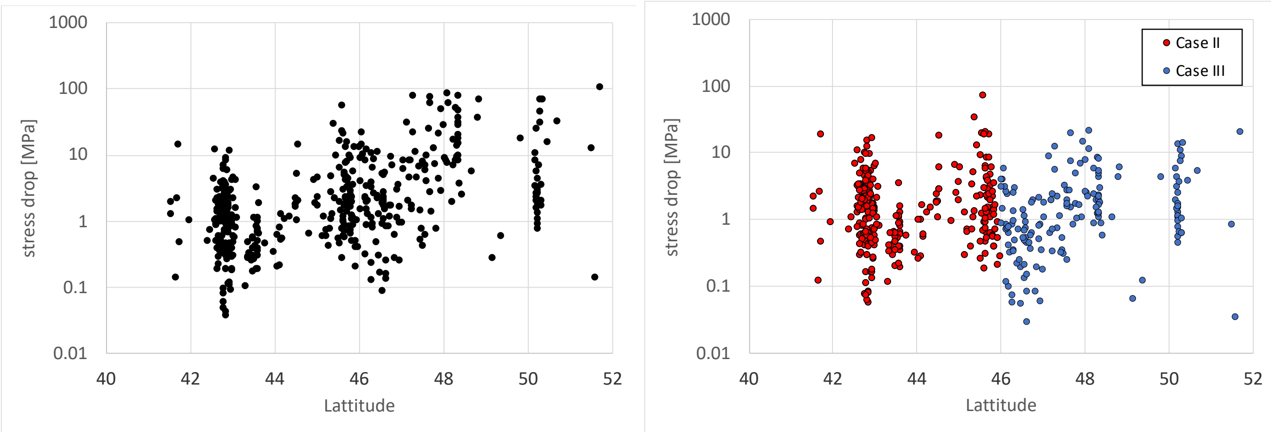

Figure 20. The distribution of the stress drops with the latitude. Black dots indicate the result of Case I. Red dots indicate the result of Case II. Blue dots indicate the result of Case III.

3) Scaling with magnitude:

The scaling of stress drop with earthquake size is still a controversial issue in seismology and earthquake source mechanics. In our study, the scaling of the stress drops with the moment magnitude (**Figure 22**) shows a weak trend (larger earthquakes show larger stress-drops). This result is consistent with the results obtained recently by Bindi and Kotha (2020).

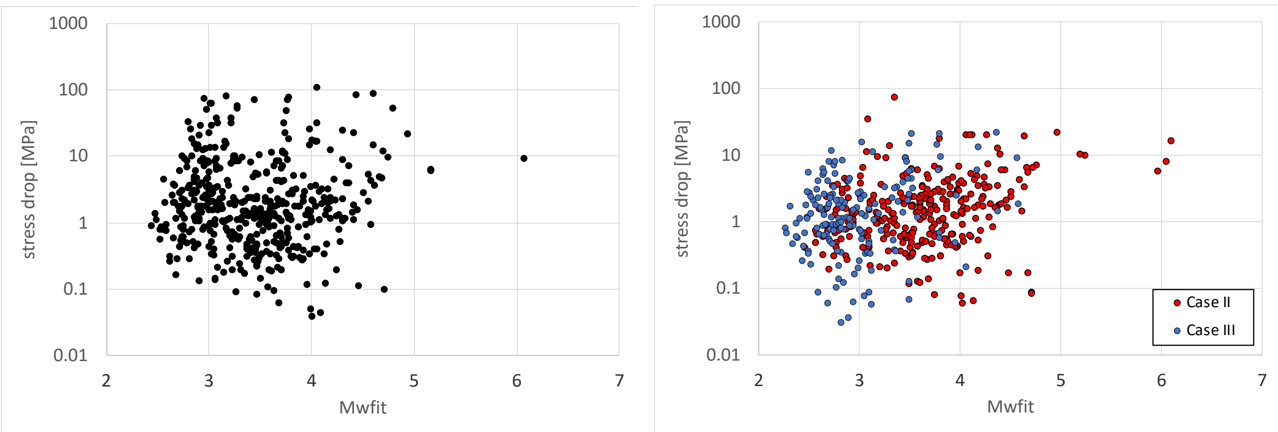

Figure 21. Stress drop scaling with moment magnitude fitting by the Brune's model. Black dots indicate the result of Case I. Red dots indicate the result of Case II. Blue dots indicate the result of Case III.

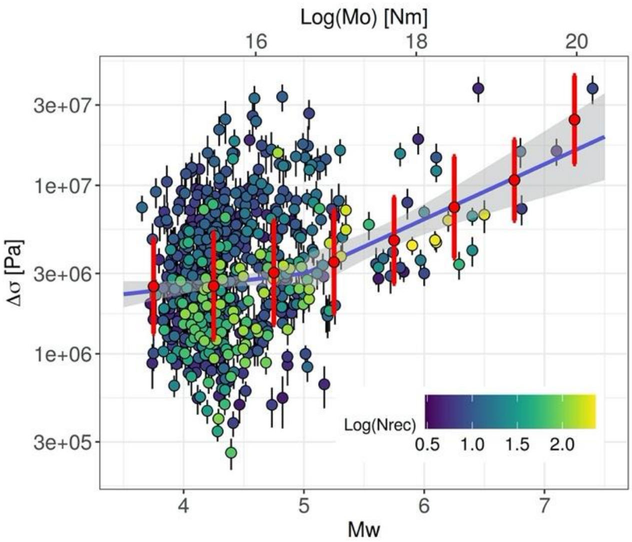

Figure 22. Variations of the stress-drop on magnitude obtained by Bindi and Kotha (2020) for European earthquakes, using data from the Engineering Strong Motion database. Red bars are the mean ± one standard deviation computed over intervals 0.5 m.u. wide; blue line is the result of a segmented regression, along with the confidence bound.

4) Variability of stress-drop:

Variability of stress-drop is important for the future usage of the ground-motion simulations. **Table 1** shows the stress drop and variability from spectral studies (Cotton et al., 2013). This table shows that various studies give different estimations of this variability which indicate the need to regionalize stress-drops analysis. In this report, we have created the framework needed to investigate into the details such a variability and compare it with the results of previous studies.

Table 1. Stress drops and variability from spectral studies (Cotton et al., 2013).

Table 1: Stress drops and variability from spectral studies (M_0, f_C)

Source study	Region	Mean Brune stress-drop ($\Delta\tau$) (MPa)	Stress-drop variability $Ln(\Delta\tau)$	No. earthquakes
Allmann and Shearer, 2009	Interplate $5.5 \leq M_W \leq 8$	0.84*	1.67	799
Allmann and Shearer, 2009	Intraplate $5.5 \leq M_W \leq 8$	1.50*	1.46	61
Oth et al, 2010	Japan (crustal) $2.7 \leq M_{JMA} \leq 8$	1.1	1.38	1951
Rietbrock et al., 2012	UK	1.8	1.38	273
Edwards and Fah, 2012	Switzerland (foreland)	0.2	1.83	161
Edwards and Fah, 2012	Switzerland (alpine)	0.12	1.43	351
Shearer et al., 2006	Southern California $1.6 \leq M_L \leq 3.1$	0.52*	1.52	64800
Margaris and Hatzidimitriou, 2002	Greece $5.2 \leq M_W \leq 6.9$	6.3	0.57	18
Johnston et al., 1994	Intraplate	10	0.7	?

*Published results are divided by 3.95 to take into account the difference between a Madariaga (1976) corner frequency/source radius compared to that of Brune (1970,1971) and the difference in shear wave velocity.

Future work

Regionalization and Parametrization

According to the results presented in this report, the attenuation functions determined when the entire region data are used is mainly controlled by the large amount of data from the latitude less than 46ºN. It suggests that a regionalization is important for getting accurate attenuation functions in low seismicity areas. We then plan to improve the regionalization scheme of the inversion framework. We also plan to modify the parametrization used in the general inversion technique. Indeed, the use of such inversions results for ground motion predictions using stochastic simulation methods (e.g., Boore et al., 2003) implies that the model of source parameters of such modeling is consistent with the output of our inversions. We plan to improve this consistency by providing source parameters which are suitable for the ground-motions stochastic simulation techniques implementing also spectral decomposition approaches based on parametric schema.

Multi-event detection

The lessons learned from this work show that the multi-event detection method can be improved. During the pre-processing, a multi-event detection was applied to the database. However, some segments with potential multi-event behavior survived and are not excluded from the present filtering method. With such huge amount and variety of data, new method and software developments are needed to reduce artificial errors in the downloading and preprocessing procedures. In order to preprocess the monitoring data flow more accurately and efficiently, we propose a method to achieve the automatic identification of the occurrence of multi-events by using deep learning techniques. Here we transform the recorded waveforms from time-domain into time-frequency representation, thereby applying Convolutional neural networks (CNN) to automatically pick out the multi-events, without manual feature extraction. Due to the need of automated data preprocessing in seismology, we programmed the proposed methodology in Python so that it could be further integrated to existing pre-processing programs, such as Stream2segment and Obspy.

Outlier detection

During the processing phase, we would like to improve the detection of "outliers". The outlier detection method used in this study was based on a simple residual analysis and this method only provides a binary classification of the processed time-histories as "outlier" or "not-outlier". An index or score assigning a subjective probability would be a better way to indicate the outlier feature of the data. The technique, Seismic Data (and metadata) Amplitude Anomaly Score, which has been recently developed at GFZ (the program available on github, https://github.com/rizac/sdaas) provides such an index of 0-1 to describe the level of outlier feature. We plan to implement such method for future applications.

Reference

Aki, K. (1967). Scaling law of seismic spectrum, J. Geophys. Res. 72, 1217–1231.

Ameri, G., Martin, C., & Oth, A. (2020). Ground-motion attenuation, stress drop, and directivity of induced events in the Groningen gas field by spectral inversion of borehole records. Bulletin of the Seismological Society of America, 110(5), 2077-2094.

Baltay, A., Ide, S., Prieto, G., & Beroza, G. (2011). Variability in earthquake stress drop and apparent stress. Geophysical Research Letters, 38(6).

Baltay, A., Prieto, G., & Beroza, G. C. (2010). Radiated seismic energy from coda measurements and no scaling in apparent stress with seismic moment. Journal of Geophysical Research: Solid Earth, 115(B8).

Bindi, D., & Kotha, S. R. (2020). Spectral decomposition of the Engineering Strong Motion (ESM) flat file: regional attenuation, source scaling and Arias stress drop. Bulletin of Earthquake Engineering, 1-26.

Brune, J. N. (1970). Tectonic stress and the spectra of shear waves from earthquakes, J. Geophys. Res. 75, 4997–5009.

Brune, J. N. (1971). Seismic sources, fault plane studies and tectonics, Eos Trans. AGU, IUGG 52, no. 5, 178, doi: 10.1029/EO052i005-pIU178.

Castro, R. R., J. G. Anderson, and S. K. Singh (1990). Site response, attenuation and source spectra of S waves along the Guerrero, Mexico, subduction zone, Bull. Seismol. Soc. Am. 80, 1481–1503.

Cocco, M., Tinti, E., & Cirella, A. (2016). On the scale dependence of earthquake stress drop. Journal of Seismology, 20(4), 1151-1170.

Cotton, F., Archuleta, R., & Causse, M. (2013). What is sigma of the stress drop? Seismological Research Letters, 84(1), 42-48.

Denolle, M. A., and P. M. Shearer (2016), New perspectives on self-similarity for shallow thrust earthquakes, J. Geophys. Res. Solid Earth, 121, 6533–6565, doi:10.1002/2016JB013105.

Drouet S., Cotton F. and Gueguen P. (2010). vS30, κ, regional attenuation and Mw from accelerograms: application to magnitude 3–5 French earthquakes. Geophys. J. Int. (2010) 182, 880–898.

Edwards, B., Rietbrock, A., Bommer, J.J.&Baptie, B. (2008). The acquisition of source, path, and site effects from microearthquake recordings using Q tomography: application to the United Kingdom, Bull. seism. Soc. Am., 98, 1915–1935.

Eshelby, J. D. (1957). The determination of the elastic field of an ellipsoidal inclusion, and related problems, Proc. Math. Phys. Sci. 241, 376-396.

Hanks, T. C. and Kanamori, H. (1979). A moment magnitude scale, J. Geophys. Res.,84, 2348-2350.

Harrington, R. M., & Brodsky, E. E. (2009). Source duration scales with magnitude differently for earthquakes on the San Andreas Fault and on secondary faults in Parkfield, California. Bulletin of the Seismological Society of America, 99(4), 2323-2334.

Haskell, N. A. (1964). Total energy and energy spectral density of elastic wave radiation from propagating faults. Bulletin of the Seismological Society of America, 54, 1811–1841.

Ide, S., & Beroza, G. C. (2001). Does apparent stress vary with earthquake size? Geophysical Research Letters, 28(17), 3349-3352.

Ide, S., Beroza, G. C., Prejean, S. G., & Ellsworth, W. L. (2003). Apparent break in earthquake scaling due to path and site effects on deep borehole recordings. Journal of Geophysical Research: Solid Earth, 108(B5).

Izutani, Y., & Kanamori, H. (2001). Scale-dependence of seismic energy-to-moment ratio for strike-slip earthquakes in Japan. Geophysical research letters, 28(20), 4007-4010.

Keilis-Borok, V. (1959). On the estimation of the displacement in an earthquake source and of source dimension, Ann. Geophys. 12, 205-214.

Madariaga, R. (1976). Dynamics of an expanding circular fault. Bulletin of the Seismological Society of America, 66(3), 639-666.

Mayeda, K., Gök, R., Walter, W. R., & Hofstetter, A. (2005). Evidence for non-constant energy/moment scaling from coda-derived source spectra. Geophysical research letters, 32(10).

Moschetti, M. P., and S. H. Hartzell (2020). Spectral Inversion for seismic site response in Central Oklahoma: low-Frequency resonances from the Great Unconformity, Bull. Seismol. Soc. Am., doi:10.1785/01202002

Oth, A., Bindi, D., Parolai, S., & Di Giacomo, D. (2011). Spectral Analysis of K-NET and KiK-net Data in Japan, Part II: On Attenuation Characteristics, Source Spectra, and Site Response of Borehole and Surface Stations Spectral Analysis of K-NET and KiK-net Data in Japan, Part II. Bulletin of the Seismological Society of America, 101(2), 667-687.

Parolai, S., D. Bindi, and P. Augliera (2000). Application of the generalized inversion technique (GIT) to a microzonation study: Numerical simulations and comparison with different site-estimation techniques, Bull. Seismol. Soc. Am. 90, 286–297.

Parolai, S., D. Bindi, M. Baumbach, H. Grosser, C. Milkereit, S. Karakisa, and S. Zunbul (2004). Comparison of different site response estimation techniques using aftershocks of the 1999 Izmit earthquake, Bull. Seismol. Soc. Am. 94, 1096.